Nuclear Engineering and Technology 51 (2019) 665–675

Contents lists available at ScienceDirect

Nuclear Engineering and Technology

journal homepage: www.elsevier.com/locate/net

Original Article

Numerical investigation on vortex behavior in wire-wrapped fuel assembly for a sodium fast reactor

Min Seop Song [a], Jae Ho Jeong [b, **], Eung Soo Kim [a, *]

[a] Department of Nuclear Engineering, Seoul National University, 559 Gwanak-ro, Gwanak-gu, Seoul, South Korea
[b] Korea Atomic Energy Research Institute, 989-111 Daedeok-daero, Yuseoung-gu, Daejeon, Republic of Korea

ARTICLE INFO

Article history:
Received 9 August 2018
Received in revised form
24 November 2018
Accepted 20 December 2018
Available online 20 December 2018

Keywords:
Sodium-cooled fast reactor
Wire-wrapped fuel bundle
Computational fluid dynamics
Vortex identification

ABSTRACT

The wire-wrapped fuel bundle is an assembly design in a sodium-cooled fast reactor. A wire spacer is used to maintain a constant gap between rods and to enhance the mixing of coolants. The wire makes the flow complicated by creating a sweeping flow and vortex flow. The vortex affects the flow field and heat transfer inside the subchannels. However, studies on vortices in this geometry are limited. The purpose of this research is to investigate the vortex flow created in the wire-wrapped fuel bundle. For analysis, a RANS-based numerical analysis was conducted for a 37-pin geometry. The sensitivity study shows that simulation with the shear stress transport model is appropriate. For the case of Re of 37,100, the mechanisms of onset, periodicity, and rotational direction were analyzed. The vortex structures were reconstructed in a three-dimensional space. Vortices were periodically created in the interior subchannel three times for one wire rotation. In the edge subchannel, the largest vortex occurred. This large vortex structure blocked the swirl flow in the peripheral region. The small vortex formed in the corner subchannel was negligible. The results can help in understanding the flow field inside subchannels with sweeping flow and vortex structures.

© 2019 Korean Nuclear Society, Published by Elsevier Korea LLC. This is an open access article under the CC BY-NC-ND license (http://creativecommons.org/licenses/by-nc-nd/4.0/).

1. Introduction

1.1. Research background

The wire-wrapped fuel bundle is a form of nuclear fuel assembly used in sodium-cooled fast reactors (SFRs). Because SFR operates in the range of fast neutron, it uses an aggregate form of a dense triangular array to reduce the deceleration and loss of neutrons. Accordingly, liquid sodium, which has 100 times higher thermal conductivity than water, is used as a coolant to efficiently transfer the thermal energy in the fuel assembly. A wire is wound around the fuel pin to enhance mixing of the coolant between the subchannels as shown in Fig. 1 (a). The wire also serves as a support grid between fuel pins.

The wire makes the flow inside the fuel bundles complicated by the following two actions. A portion of the axial flow sweeps along the wire and turns into a transverse flow [1]. Another part of the axial flow, on the other hand, creates a vortex structure by flow separation over the wire [2].

In order to understand the characteristics of the transverse flow in the wire-wrapped fuel bundle, it is necessary to identify the effect of the wire on the transverse flow. The sweeping flow is influenced by the direction and angle of the wire, and it explains the flow direction between subchannels. On the other hand, the vortex changes the flow field inside the subchannel. In addition, the vortex has an influence on the local heat transfer and temperature distribution at the cladding surface [2]. Therefore, analyzing the vortex structure can be very helpful in understanding the flow and heat transfer characteristics of the coolant inside the fuel bundles. However, detailed studies on the characteristics of vortices generated inside subchannels are rare. Therefore, numerical analysis studies have been conducted to determine the characteristics of vortices generated in wire-wrapped fuel bundles.

1.2. Previous research

There are many experimental and analytical studies on the flow pattern and structure in wire-wrapped fuel bundles. Each study was conducted using different geometric parameters according to the purpose of the experiment.

* Corresponding author.
** Corresponding author.
E-mail addresses: jhjeong@kaeri.re.kr (J.H. Jeong), kes7741@snu.ac.kr (E.S. Kim).

https://doi.org/10.1016/j.net.2018.12.012
1738-5733/© 2019 Korean Nuclear Society, Published by Elsevier Korea LLC. This is an open access article under the CC BY-NC-ND license (http://creativecommons.org/licenses/by-nc-nd/4.0/).

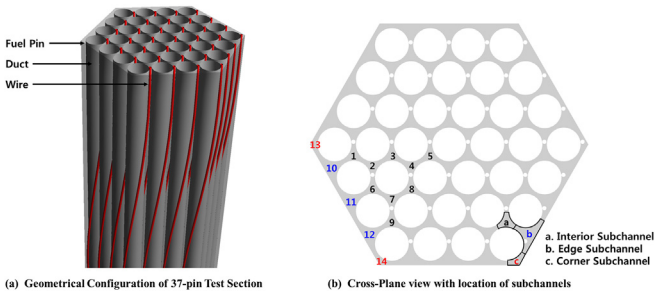

Fig. 1. Geometry of 37-pin test section and subchannels.

Ranjan et al. simplified the wire-wrapped pin geometry to a wire on a plane and performed a direct numerical simulation (DNS) study [2]. They found that the vortex (recirculation bubble) was generated by flow separation at the back of the wire, and the secondary bubble was generated in the narrow space between the plane and wire. It was also found that a high-temperature region existed at the secondary bubble due to thermal confinement. This phenomenon was also reported by Jeong et al. in their numerical analysis result on the liquid sodium flow for a 7-pin wire-wrapped fuel bundle [3]. In the backside of the wire, the wire and the transverse flow created a wake, which had a slow axial velocity region. The increase in temperature in the wake region corresponded to 5% of the temperature difference between the inlet and outlet.

Jeong et al. also showed the presence of a vortex near the wire through a Reynolds-averaged Navier–Stokes (RANS)-based computational fluid dynamics (CFD) analysis of a 217-pin SFR fuel bundle [4]. According to this research, a small-scale vortex occurred in the interior subchannel, whereas a large-scale vortex existed in the edge and corner subchannels. The occurrence of these vortices was related to the position of the wire.

Gajapathy et al. investigated the change in flow characteristics with respect to the number of pins by comparing the CFD results with 7-, 19-, and 37-pin assemblies. They confirmed the expandability of the analysis result to more pins. Normally, a large swirl flow induced by the wire in the peripheral subchannels was observed irrespective of the number of pins. At the same time, cross-sectional vortices rotating at opposite direction to the wire rotation were observed [5].

The presence of vortices was confirmed not only by numerical analysis but also by experiments on the flow in wire-wrapped fuel bundles. Ohtake et al. obtained the velocity vector fields in a test section of a 37-pin wire-wrapped fuel bundle with a 5-way pitot tube [6]. This pitot tube intrusively measured 3-D velocity vectors. The results showed that when the wire passed through the interior and edge subchannels, a vortex that rotated in a direction opposite to the wire existed. In addition, the vortex occurred at the downstream of the wire in the interior subchannel. The axial flow in the vortex regions was rather small. The transverse flow between subchannels was related to the flow resistance induced by the wire.

Nishimura et al. observed the presence of vortices in the interior subchannel through 3-pin flow visualization experiments with particle image velocimetry (PIV) [7]. The transverse flow field was obtained by synthesizing the PIV data. It was confirmed that the vortex occurred in the downstream of the wire. This qualitatively agreed with the flow field observed in the SPIRAL code [8].

The following conclusions can be made from these previous studies. The existence of vortices has been confirmed by experiments and simulations. The occurrence of vortices depends on the relative position of the wire, not on the geometric parameters such as the pin pitch to pin diameter ratio and number of pins. In addition, vortices occur in the downstream of the wire and they rotate in the opposite direction of the wire rotation. Although previous studies reported their existence, detailed analyses of vortex structures and their occurrence patterns are limited. To understand the flow characteristics in the fuel bundle, it is necessary to thoroughly understand the vortex structures in the flow.

1.3. Research purpose and scope

This research aims to analyze in detail the vortex structures generated in each subchannel. It includes the generation mechanism and location of the vortex. The size and occurrence frequency were also investigated. To simulate the flow in the wire-wrapped fuel bundle, a RANS-based steady-state CFD analysis was performed. With the development of CFD techniques with RANS-based turbulence models and the computing power that reduces calculation costs, it became possible to simulate and investigate flow structures in complex geometries by constructing detailed grid structures. The test section for the CFD study was based on the Prototype Gen-IV Sodium-cooled Fast Reactor (PGSFR)-based 37-pin model designed by Korea Atomic Energy Research Institute (KAERI) [9]. The pressure drop data provided in the article were compared with the CFD result for validation. To figure out the vortex generation pattern in each subchannel, streamlines were drawn at the planes of different heights. Vortex identification parameters were adopted to detect the vortex structure and identify its size and range. Finally, the 3-D vortex structures in every subchannel were reconstructed and analyzed.

2. Numerical methodology

2.1. Model geometry and flow conditions

In this study, a numerical analysis of the flow in the 37 wire-wrapped fuel bundle was performed. Previous studies have reported that when the number of pins is higher than 19, the effect of the number of pins on the flow distribution weakens [5,10]. Therefore, among the various experimental cases, the KAERI SFR 37-pin flow experiment, which was based on the design parameters of PGSFR, was selected as the benchmark design [9]. This experiment was performed with water to obtain benchmark data for subchannel codes. It provided not only the detailed geometric parameters but also the pressure drop and mass flow rate at the outlet measured with a differential pressure meter and an isokinetic sampling probe. Friction factors calculated from the pressure drop measurements provided the overall flow resistance on Reynolds number, which was necessary for the validation of CFD studies.

The test section for CFD was constructed based on the geometry of the KAERI SFR 37-pin model. In the 37-pin test section, 54 interior subchannels, 18 edge subchannels, and 6 corner subchannels exist. The shape of each subchannel is shown in Fig. 1 (b). The wire rotates clockwise from the inlet. The basic design parameters, P/D_P and L/D_P, of this model are 1.13 and 27.69, respectively. D_P is 8 mm and D_W is 1 mm. The diagonal of the hexagonal duct is 66 mm wide. The hydraulic diameter (D_h) is calculated as 3.04 mm for the inlet cross-section with the inlet area of 944.7 mm^2. As the total height (H_T) is 1500 mm, the wire rotates 6.77 times with one pitch length (L_W) of 221.5 mm. Previous studies revealed that the axial flow field in the SFR core is developed after two turns of wire, while the lateral flow field is developed after approximately three turns [5,11]. Therefore, this test section is long enough to attain a developed flow.

The experiment was conducted with water at 60 °C and a system pressure of 4 bar [9]. The temperature of the water was

increased to lower its viscosity. The density (ρ) of water in this condition was 983.4 kg/m^3 and the dynamic viscosity (μ) was 4.67 × 10^{-4}kg/(m•s). The low dynamic viscosity enables the experimental condition to be easily adjusted to the operational Reynolds number of PGSFR without increasing the pumping power. The operational Reynolds number of PGSFR is approximately 37,100 for sodium. The experiments were conducted from 20% to 115% of the operational Reynolds number. The same inlet mass flow rate was applied to the CFD as presented in Table 1.

2.2. Computational grid system

The constitution of the grid system is based on the design process developed by Jeong et al. [12,13] In this grid system, the flow field is divided by an interior and an outer region. The interior region includes the pin and wire, and the outer region consists of the remaining components. Both regions are composed of a structured grid. The grid of the interior region maintains high quality by rotating the grid with the wire (Fig. 2). This allows the grid near the pin and wire to have high quality with fewer grids, and the flow near the wire can be accurately calculated. The unmatched nodes between the regions were treated by the general grid interface (GGI) option of ANSYS-CFX. The analytical simulation results with this methodology have already proven that a highly accurate prediction of pressure drop is possible with a low computational cost [12,13]. A total of 7 million grids were used for the grid configuration. By simulating the entire test section of 6.77 laps, the flow could have a very long developmental length compared to the cross-sectional hydraulic diameter. Therefore, it is possible to avoid the flow disturbance effect at the inlet and outlet as much as possible. At the flow condition of Reynolds number of 37,830, y$^+$ was kept below 2 in most areas.

2.3. Numerical method

In this analysis, the CFX 17.0 of ANSYS, a commercial computational fluid dynamics program, was used [14]. CFX implements calculation of mass, momentum, and energy equations for fluid flow based on the finite volume method. The inlet boundary conditions were set as the mass flow rate used in the benchmark experiment as listed in Table 1. An average static pressure of 0 was applied at the outlet. Both the advection scheme and turbulence numerics had the high-resolution option. Iterations were performed 500 times, and the calculated root mean square (RMS) residual values of momentum and pressure converged below 10^{-4}. We also monitored the change in the area-averaged pressure value at the outlet and confirmed that the values converged sufficiently after the iterations. The turbulence models used in the analysis were SST, k-ω, EARSM, RNG k-ε, k-ε, and LRRSM models [14]. For the non-low Reynolds number turbulence model, the wall function was applied.

2.4. Sensitivity study

The grid sensitivity study on the scale of the first grid at the wall was conducted with friction factor in Eq. (1). The friction factor was

Table 1
Inlet boundary conditions.

	Percentage (%)	Re	Mass Flow Rate (kg/s)
1	20	7420	1.09
2	50	18,550	2.75
3	72	26,712	3.95
4	100	37,100	5.49
5	115	42,665	6.31

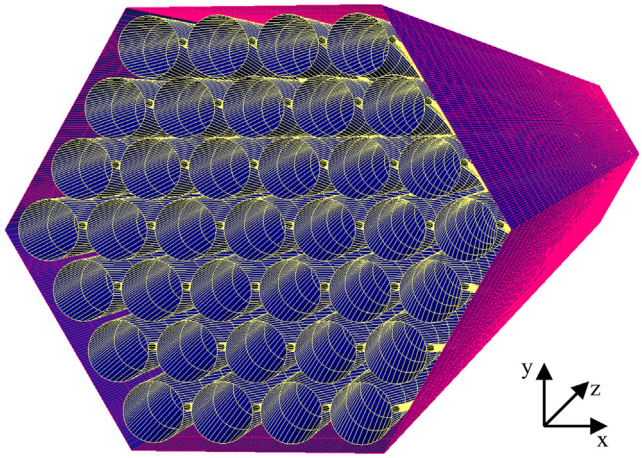

(a) Wire Wrapped Fuel Bundle and Duct

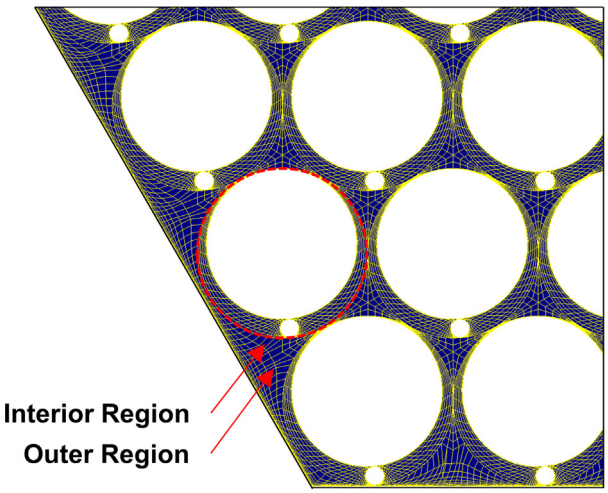

(b) Cross Plane

Fig. 2. Grid structure of test section.

calculated from the pressure drop data obtained at the measurement points specified in Chang's experiment [9]. The distance between pressure taps (L) was 664.5 mm [9]. To calculate the friction factor at the interior subchannel, the hydraulic diameter ($D_{h,i}$ = 2.70 mm) and bulk velocity at the interior subchannel were applied. The bulk velocity in the interior subchannel was 0.5% lower than the bundle bulk velocity.

$$f = \Delta P \cdot \frac{D_{h,i}}{L} \cdot \frac{2}{\rho U_i^2} \quad (1)$$

The y$^+$ of the grid was changed as 1, 2, and 5. For the turbulence model, the SST model was used because it accurately predicted the pressure drop in the wire-wrapped fuel bundle in previous studies using the same numerical methodology [4,13].

Fig. 3 shows a graph for the comparison of the friction factor between the experimental data and the CFD results at Re values of 27,218, 37,830, and 43,481. Among the experimental results, the friction factor at subchannel 31 was used. The difference between

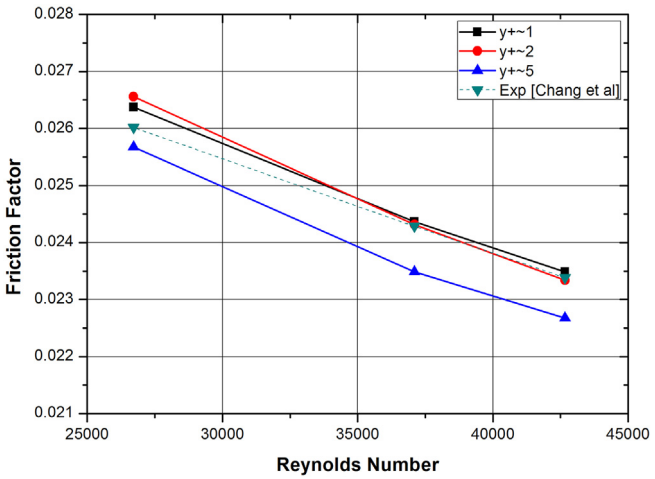

Fig. 3. Grid sensitivity test result.

the experiment and CFD is smaller than 0.001 in the entire range. As y^+ becomes smaller, the experimental data and analysis results become closer, and the difference between y^+ of 1 and 2 is negligible. From this result, it can be concluded that the grid structure with $y^+ = 1$ is an appropriate case to simulate the 37-pin wire-wrapped pin test section.

Additionally, a sensitivity analysis on the turbulence model was performed. Fig. 4 compares the friction factor calculated from various turbulence models for the entire Re range with experimental results. Consequently, the analytical results using the k-ω and SST models were in good agreement with the experimental results. Among them, the SST model showed better agreement for Reynolds number ranges that were higher than 20,000. The results of the friction factor prediction for the models based on k-ε and RSM were slightly lower than the experimental results. This was attributed to the complex and narrow flow passage in the wire-wrapped fuel bundle. Because the subchannel area is surrounded by the pin, wire, and duct, many parts belong to the boundary layer. Therefore, the turbulence model based on k-ω is more accurate because it solves the near-wall velocity field for this complex geometry without wall function. This result was found to be consistent with that of the aforementioned studies.

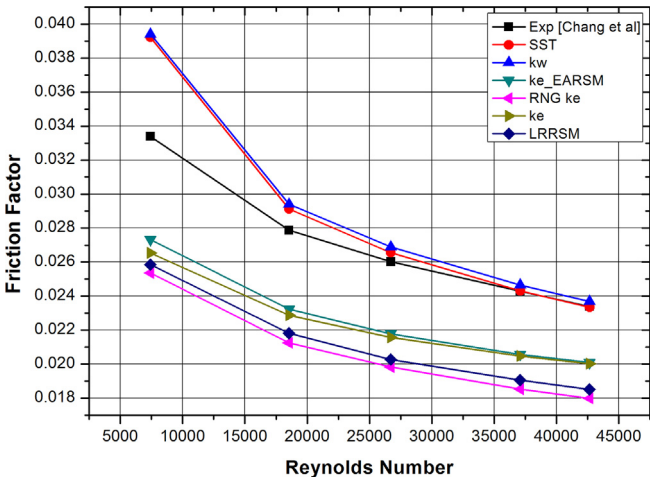

Fig. 4. Friction factor comparison for different turbulence model Figure D. Change of edge vortex position with wire position.

2.5. Verification of flow field

The validity of the analysis results can be confirmed by comparing the global flow patterns with those obtained in previous studies. The distinct flow patterns observed in the wire-wrapped fuel bundle are the large swirl flow in the peripheral region and the uniformity of flow fields in the internal subchannels [5,13,15]. Fig. 5 shows the contours of axial velocity with the streamline of the transverse flow as the angle of the wire progressed by 60°. Basically, the axial velocity is higher in the edge subchannel than that in the interior subchannel. In addition, the streamline and axial velocity in the interior subchannels have a similar pattern irrespective of the position of the interior subchannel. A large swirl flow, which rotates with the wire, is also observed in the outermost region. These flow patterns are also observed in other simulation results regardless of the geometric parameters.

3. Characteristics of vortex behavior

3.1. Onset of vortex

The vortex structures in the wire-wrapped fuel bundle occur as the flow is blocked by the wire. Fig. 6 shows the contour of the pressure field and streamline at the cross-plane along with the z-direction when the wire passes through the interior subchannel. The main flow inside the wire-wrapped fuel bundle is axial flow, and the wire exists as an inclined obstacle to the axial flow. The part where the wire meets the main flow is called the wind side, and the opposite side is the lee side. The pressure of the wind side becomes higher than that of the lee side due to the flow blockage. While the wire is passing the interior subchannel (P1 to P5), some of the main flow traveled over the wire and is converted to a large vortex (V1). This type of vortex (V1) can be named as center vortex as it is located in the center of the subchannel. The rotational direction of the V1 vortex becomes opposite to the wire rotation. These properties of vortices in wire-wrapped fuel bundles were already observed by Ohtake and Nishimura in their experimental studies [6,7]. They occur whenever the main flow meets a wire in every subchannel. The length scale of the vortex depends on the width of the subchannel and transverse flow. The other vortex created in the subchannel is the back vortex (V2). It is created by the transverse flow behind the wire. The back vortex is continuously confined between the surface of the pin and wire at a small scale.

3.2. Vortex identification methods

In this study, we adopted two vortex identification parameters, namely helicity and Q-invariant, to distinguish the vortex structures from the flow field [16]. These parameters are used to visualize the vortex in wire-wrapped fuel bundles and to identify the onset frequency and swirl strength. Helicity is defined by Eq. (2). It discriminates the direction and strength of the vortex. Normalized helicity (Eq. (2.1)) determines the directionality between the

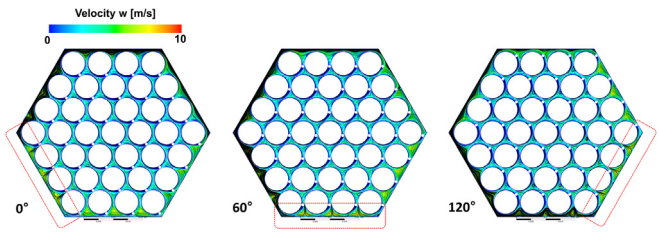

Fig. 5. Variation of the flow pattern with wire angle.

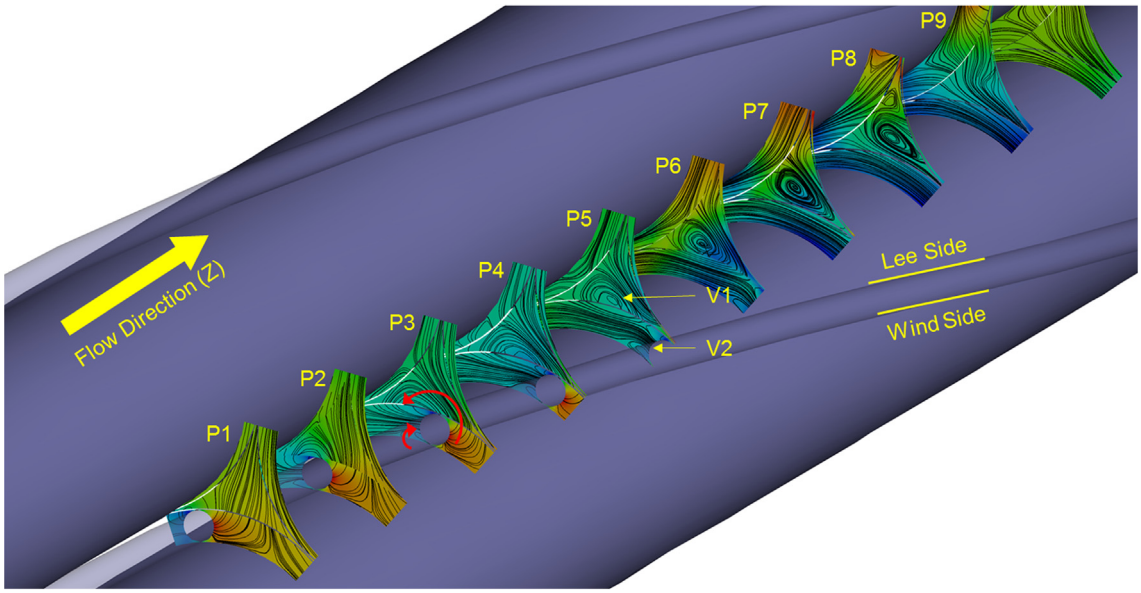

Fig. 6. Generation and Destruction of Vortices around Wire in Interior Subchannel (Contour: Local pressure field, Red: High, Blue: Low).

velocity vector and the vorticity. Helicity is positive when the velocity vector and the curl vector have the same direction of rotation. As the axial flow is dominant in the wire-wrapped rod test section, the sign of helicity can determine the rotational direction of the vortex.

$$H = \int_V \boldsymbol{u} \cdot (\nabla \times \boldsymbol{u}) dV \tag{2}$$

$$H_{nor} = \int_V \frac{\boldsymbol{u} \cdot (\nabla \times \boldsymbol{u})}{|\boldsymbol{u}||(\nabla \times \boldsymbol{u})|} dV \tag{2.1}$$

Q-invariant is defined as the second invariant of the velocity gradient tensor (Eq. (3)). It is calculated as the local balance of rate of rotation and rate of strain. A positive Q-invariant means that the rate of rotation is higher than the rate of strain, which indicates a high probability of the existence of rotational flow. The local peak of the Q-invariant could indicate a core of the rotational flow.

$$\begin{aligned} Q &= \frac{1}{2}\left(\Omega_{ij}^2 - S_{ij}^2\right) = -2\frac{\partial u_i}{\partial x_j}\frac{\partial u_j}{\partial x_i} \\ \Omega_{ij}(Rate\ of\ rotation) &= \frac{1}{2}\left(\frac{\partial u_i}{\partial x_j} - \frac{\partial u_j}{\partial x_i}\right) \\ S_{ij}(Rate\ of\ strain) &= \frac{1}{2}\left(\frac{\partial u_i}{\partial x_j} + \frac{\partial u_j}{\partial x_i}\right) \end{aligned} \tag{3}$$

3.3. Vortex analysis with helicity and Q-invariant

In order to verify the applicability of the vortex identification parameters, the contours of velocity w, helicity, and Q-invariant for the cross-sectional plane are constructed as shown in Fig. 7. In Fig. 7 (a), the center vortex (V1) generated by the wire and the back vortex (V2) are located near the wire. V2 is created because the transverse flow behind the wire is confined between the wire and pin. It can be observed that the axial flow in V2 is much lower

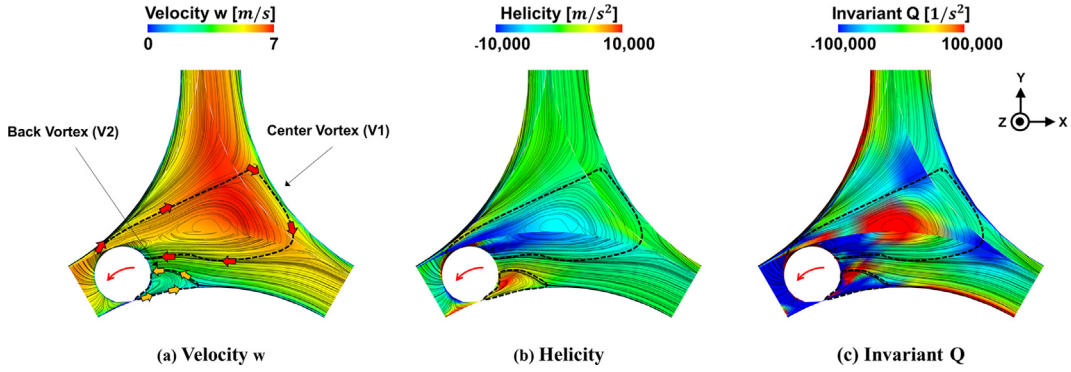

Fig. 7. Cross-plane vortex visualization at the interior subchannel.

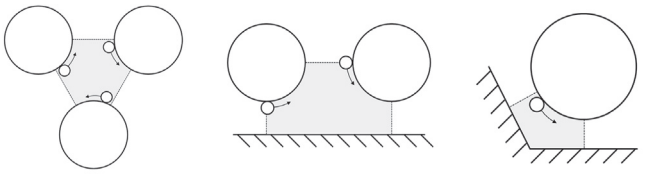

Fig. 8. Wire rotation patter by each subchannel.

compared to that in V1. V1 appears as a broad negative helicity region, which means that it turns clockwise. On the other hand, the helicity in the V2 region has a positive value as it rotates counter-clockwise. In Fig. 7 (c), it can be observed that the center of the vortices identified by the streamline matches with the peak of the Q-invariant. From this observation, it was verified that the vortex parameters could accurately show the flow direction and center of the cross-sectional vortices.

3.4. Vortex quantification in subchannel

The subchannel in the wire-wrapped fuel bundle is divided into the interior subchannel, edge subchannel, and corner subchannel as shown in Fig. 8. Because each subchannel has a different spatial composition, the pattern of wire rotation in the subchannel is also different. The helicity and Q-invariant of flow at the center of each subchannel were investigated to figure out the relationship between the location of wire and occurrence of center vortex. Target subchannels are marked in Fig. 1 (b).

3.4.1. Interior subchannel

The interior subchannel is an area surrounded by three pins in the triangle as shown in Fig. 8 (a). The wire on the pin passes through the interior subchannel 3 times per wire pitch with an equal phase difference. The center vortex (V1) is created in the interior subchannel whenever the wire passes. The helicity and Q-invariant plots in Fig. 9 show the variation in vortex parameters at each interior subchannel. The interior subchannels are divided into 1, 3, 5, 6, 8, 9 (inverted triangular area) and 2, 4, 7 (triangular area) according to the subchannel type. Two divided regions have a phase difference of 60°. The plots show that the center vortices are created three times per wire pitch. The periodic length of the helicity and Q-invariant plots is 73.8 mm, which is exactly 1/3 of 221.5 mm (L_W). Therefore, inside of the interior subchannel, the vortex occurs equally three times per cycle in association with the position of the wire.

The profile of plots coincides for the same subchannel type because the flow field in each interior subchannel is almost the same regardless of the subchannel number. A minor difference is found between Locations 2, 7, and 4. It is due to the distance of the subchannel from the core of the test section.

From the comparison between the helicity and Q-invariant plots, the flow characteristics of the vortex inside the interior subchannel can be more apparent. For example, at Z = 0.6 m, the helicity has a peak of 5,500, and the Q-invariant has a positive peak of 150,000. This is consistent with the planes in Fig. 7. The fact that the Q-invariant has a positive peak means there is a high probability that a center vortex exists. The negative helicity indicates that the rotational direction of the vortex is clockwise. The intensity and sign of the peaks appearing in other heights are almost identical. The peak values of the vortex parameters in Fig. 9 seem to converge after z = 0.8 as the flow developed.

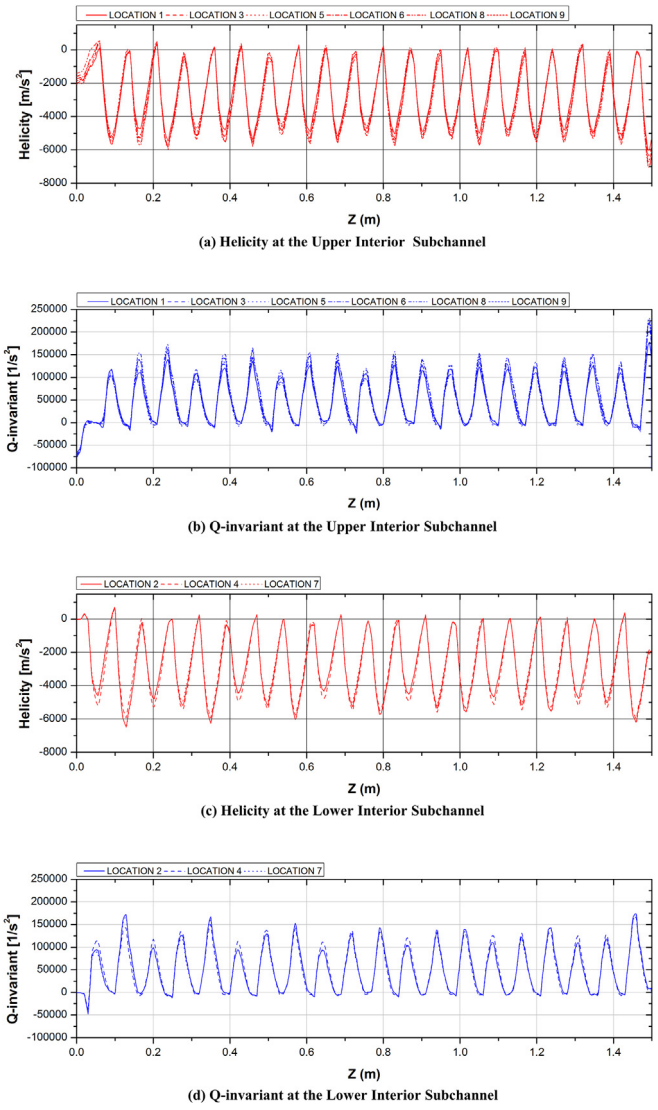

Fig. 9. Helicity and Q-invariant plot at interior subchannels.

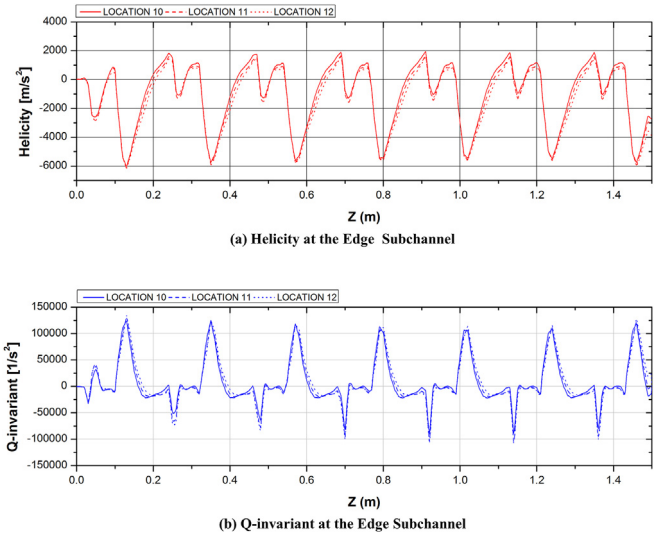

Fig. 10. Helicity and Q-invariant plot at edge subchannels.

3.4.2. Edge subchannel

The edge subchannel is surrounded by the duct wall and two pins. For one wire pitch, the wire passes through the edge subchannel twice as shown in Fig. 8 (b). The wire passes from the edge subchannel to the interior subchannel and vice versa. The different passes of these wires make the shape of the vortex structures in the edge subchannel distinct.

The helicity and Q-invariant at the center of the edge subchannels of 10, 11, and 12 are examined as shown in Fig. 10. The edge subchannels that share the same duct wall do not show phase differences (Locations 10, 11, and 12). The plots verify that the profile of the vortex parameters at each position nearly coincides with each other. Moreover, the profile of each peak is repeating from the beginning of the test section as shown in the plots in Fig. 9.

In the interior subchannel, three vortices are generated for one wire pitch, whereas one positive Q-invariant peak appears per wire cycle in the edge subchannel as shown in Fig. 10 (b). In addition, a negative peak of Q-invariant is observed, which means that the strain rate of flow is much larger than the rotation rate of flow. To examine the flow structure inside the edge subchannel in detail, contours of velocity w, helicity, and Q-invariant are shown in Fig. 11. At the planes of z equal to 1.00 and 1.02 m, where the positive peak of Q-invariant is observed, the wire turns from the edge subchannel to the interior subchannel. In this case, the large center vortex, which has a length scale of the edge subchannel, is created at the center of the edge subchannel. The negative helicity indicates that V1 rotates clockwise. In addition, the back vortex appears behind the wire. As the wire blocks the large swirl flow at the edge subchannels when it passes the gap between the duct wall and pin, the vortex grows in a large scale with less resistance. With reduced transverse flow, the axial velocity in the edge subchannel is accelerated.

In contrast, the streamlines in planes (c) and (d) show that only a small center vortex (V1) is created around the wire compared to that in (a) and (b). The large swirl flow is more dominant than the vortices. When the wire enters the edge subchannel, the transverse flow is dominant in the edge subchannel, and it acts as a resistance. Thus, in this case, the wire could not produce a large center vortex. Additionally, the magnitude of axial flow becomes smaller compared to that in (a) and (b) due to the stronger transverse flow. The helicity in the vortex is still negative.

These two distinct flow patterns provide information that the flow field is not just determined by the area of subchannel and location of wire. Although the wire occupies the same area in the subchannel, the flow pattern is different owing to the effect of transverse flow in the edge subchannel. Thus, the wire phase should be considered when modeling the flow distribution in the edge subchannels.

3.4.3. Corner subchannel

The helicity and Q-invariant are investigated at the center of the corner subchannels of 13 and 14 as shown in Fig. 12. As the corner subchannels are located at each vertex of the duct wall, they have a wire phase difference of 60° with each other. The helicity and Q-

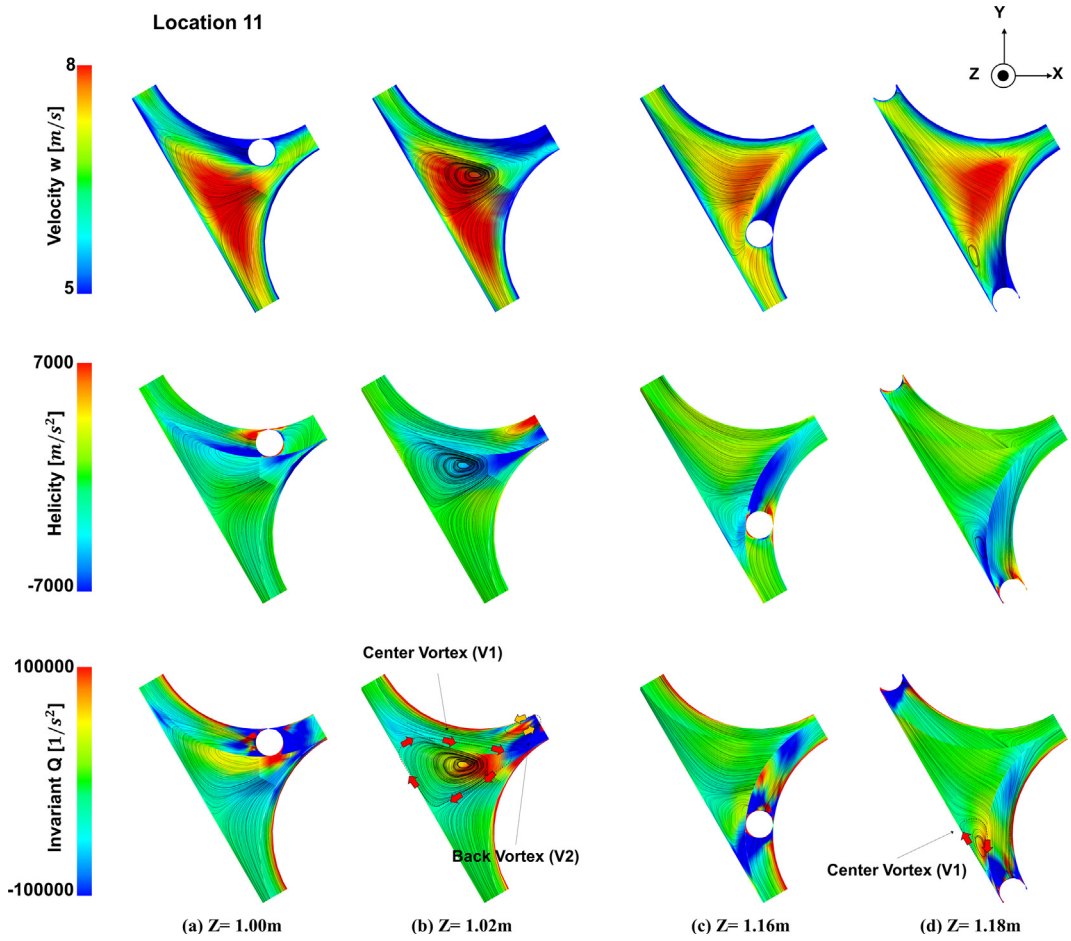

Fig. 11. Cross-plane vortices visualization at the edge subchannel.

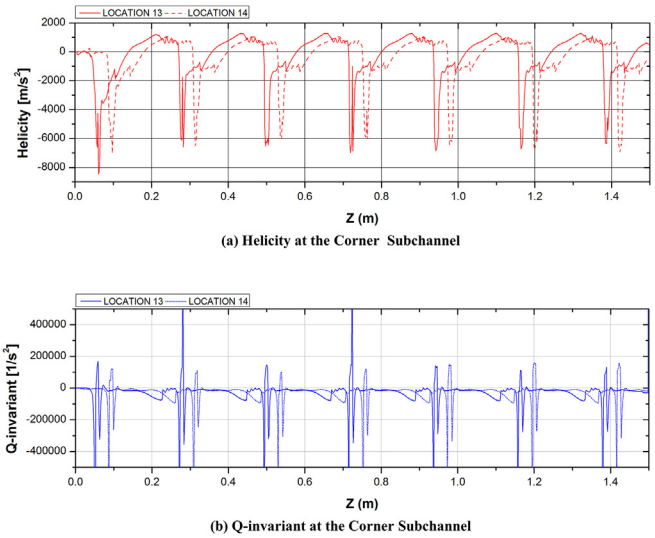

Fig. 12. Helicity and Q-invariant plot at corner subchannels.

invariant plots in Fig. 12 show that the phase of the vortex parameters at each position differs by 60° as well. In the corner subchannel, one positive Q-invariant peak appears per wire pitch. The range of peak is very narrow as the corner subchannel has a small length scale. When the vortex does not exist, the swirl flow is dominant. At the moment that the center vortex is formed (when Q-invariant is positive), the helicity becomes negative similar to that in other subchannels.

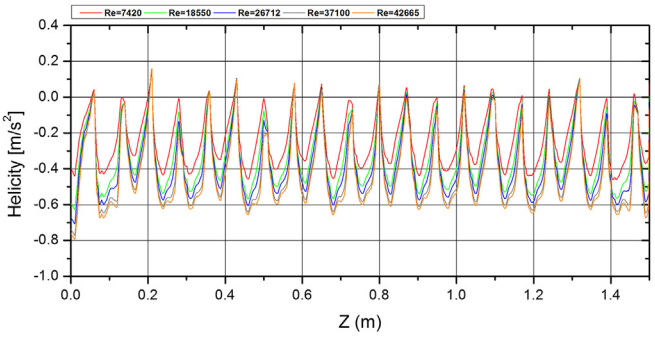

Fig. 13. Normalized helicity with different Reynolds number.

3.4.4. Effect of flow condition

The change in the normalized helicity in the interior subchannel with the Reynolds number can be examined using Fig. 13. The plot shows that the frequency of the helicity peak is the same regardless of the helicity. However, the profile at the peak changes for the higher inlet mass flow. With the increase in inlet velocity, the absolute value of the normalized helicity at the peak converges to 0.6, which means that the angle between the vector of the main flow and the vorticity vector becomes constant. Thus, the change in the Reynolds number does not significantly alter the direction and pattern of flow in the subchannel.

3.5. Elucidation of 3-D vortex structures

The analysis results in Section 3.4 focused on the location of center vortex and its directionality. It is necessary to understand the entire vortex structure that exists in the subchannels including V2. Thus, the 3-D vortex structures were reconstructed. The 3-D vortex structure was resurfaced from the isosurface of Q-invariant of 30,000. These isosurfaces were clipped again with a normalized helicity higher than 0.5 and lower than −0.5, and it showed the most appropriate result for identifying V1 and V2. XY planes contoured with the Q-invariant were added with the streamlines.

3.5.1. Interior subchannel

As shown in Fig. 8 (a), the wire passes the interior subchannel three times per wire height. It is revealed that the helicity plot has uniform peaks for equidistant z-locations, which means that the center vortex is repeatedly created in the interior subchannel. Therefore, reconstruction of the 3-D vortex is carried out for z = 1.015–1.081 m, which corresponds to one-third of the wire pitch. Fig. 14 shows the reconstruction result in this range. In Fig. 14 (a), one can observe the center vortex (V1) over the wire. The core of the vortex is identified by the streamline and contour of Q-invariant. V1 is created immediately after the wire enters the subchannel, and it falls apart to the center of the interior subchannel after the fourth plane. After the wire passes, the vortex moves to the surface of R2 and breaks.

The isosurface of the positive normalized helicity in Fig. 14 (b) shows the back vortex (V2) behind the wire. V2 continuously follows the lee side of the wire. The vortex develops to a length scale of the wire diameter. As this vortex is locked in the narrow region with low axial velocity, a local hot spot could be created.

The cross-sectional streamlines represent the direction of the transverse flow in the interior subchannel. At plane 1, the transverse flow originates from gap R1–R2 and flows into R2–R3. This

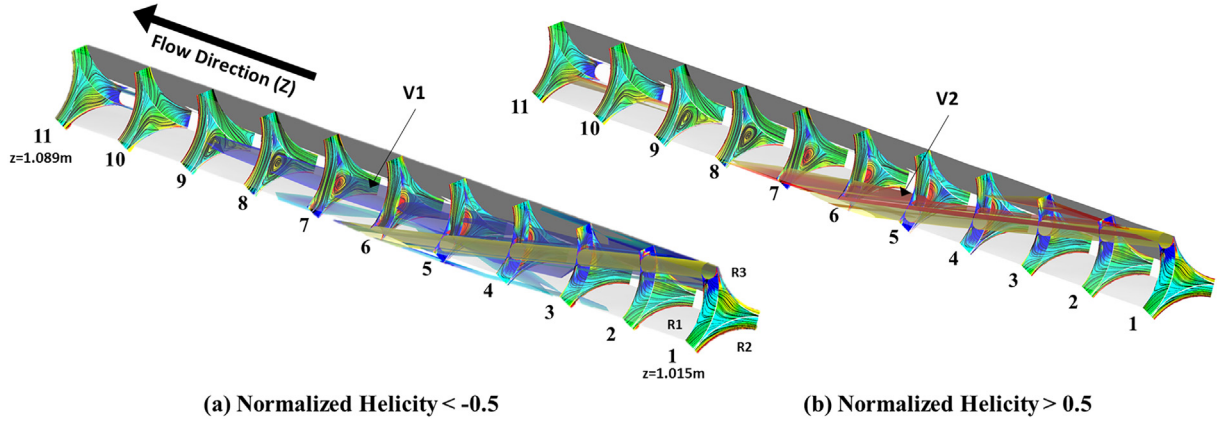

Fig. 14. Iso-surface of Q-Invariant of 30,000 at the interior subchannel.

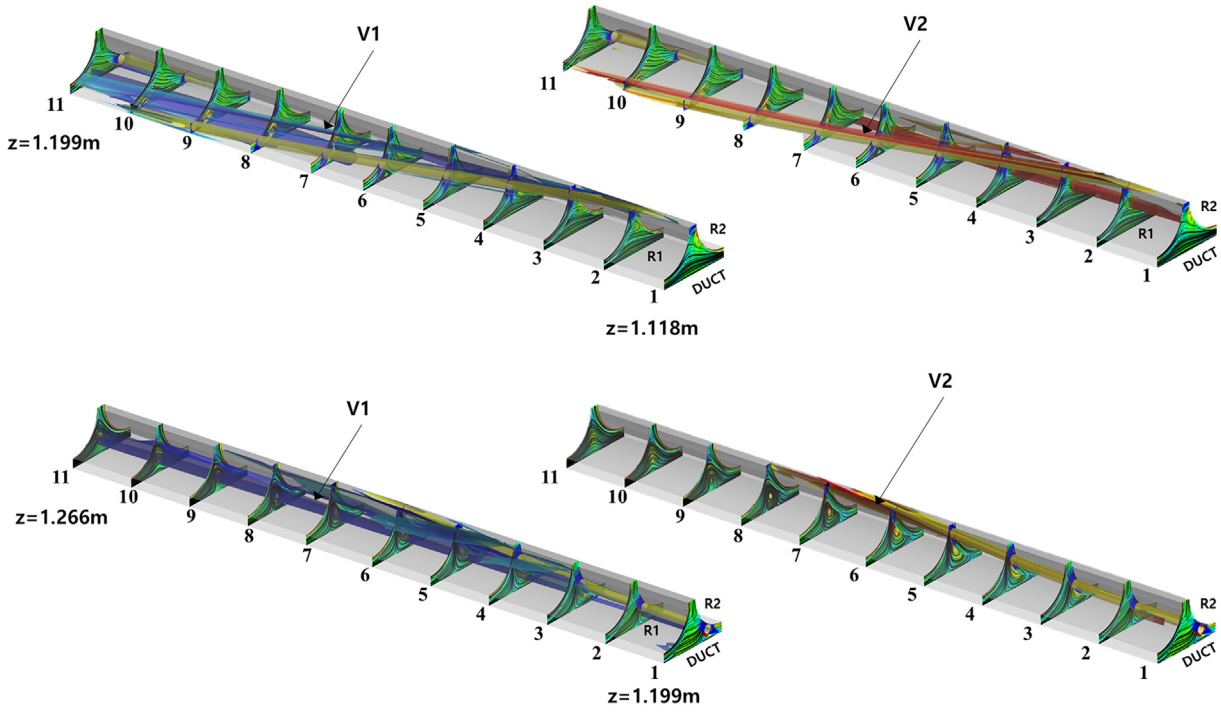

Fig. 15. Iso-surface of Q-Invariant of 30,000 at the edge subchannel.

directionality is maintained until the wire passes gap R1–R2. After the wire passes, the transverse flow heads to R1–R2, and the vortex breaks at the surface of R2. This flow pattern is consistent with the experimental results of Ohtake [6]. The author found that the transverse flow goes to the gap that is located opposite to the wire surface. After the wire passes, the transverse flow follows the lee side of the wire.

3.5.2. Edge subchannel

It was found that the flow field in the edge subchannel has two different flow patterns due to the diametrical wire rotation. In Fig. 15, the z = 1.118–1.199 m part corresponds to the region where the wire moves from the interior subchannel to the edge subchannel, and the z = 1.199–1.266 m part is the region where the wire rotates from the edge subchannel. In Fig. 11, we found that the large center vortex (V1) is created when the wire rotates from the edge subchannel to the interior subchannel. In Fig. 15, the same large V1 type vortex is observed in the z = 1.199–1.266 m region. After the wire passes the subchannel, the V1 vortex merges with the swirl flow. The maximum size of V1 reaches the distance between the duct wall and gap to the interior subchannel. In the z = 1.118–1.199 m region, the vortex did not enlarge because the strong swirl flow disturbs it. Therefore, only small vortex structures are generated in this period. The V2 vortices appear in the isosurface of the positive normalized helicity. These vortices are created in the space between the wire and the pin along the wire.

The pattern of transverse flow in the edge subchannel is as follows. The vortex (V1) in z = 1.118–1.199 m does not change the dominant swirl flow direction. On the other hand, in the downstream, the large vortex temporarily blocks the swirl flow. Thus, the large swirl flow is temporarily not created in the edge subchannel. Moreover, the axial flow in this region accelerates with a weakened transverse flow.

3.5.3. Corner subchannel

In the corner subchannel, the wire passes the subchannel once for one wire pitch, and a vortex is created only when the wire passes the corner subchannel as observed in Fig. 12. Thus, the vortex structure only at z = 1.132–1.206 m, where the wire passes the corner subchannel, is depicted in Fig. 16. In Fig. 16 (a), the vortex of V1 type is generated and developed when the wire passes the corner subchannel. The length scale of the corner vortex is smaller than the corner size. It is confined in the narrow region between the corner wall and the dominant swirl flow in the peripheral region. After the wire exits the subchannel, the vortex breaks at the corner without any change in location. In the meantime, the swirl flow continuously passes through the corner subchannel, and the flow direction at the gap of the corner subchannel is not altered by the vortex. Fig. 16 (b) shows the vortex of V2 type. V2 appears along the wire and it does not develop into a wire scale similar to the back vortex in the interior subchannel. As the two vortex structures do not have a significant effect on the transverse flow, the flow direction at the gap of the edge subchannel is identical to that of the large swirl flow.

4. Conclusions

In this study, the flow characteristics and the effects of vortex structures were investigated. The test section was made based on a 37-pin wire-wrapped fuel bundle. In order to distinguish the fine and complicated flow structure near the wire, a grid system with GGI option was used. From the sensitivity studies, it was found that the analysis case with the grid system of $y^+ = 1$ and SST turbulence model most accurately predicts the pressure drop for the range of Reynolds numbers higher than 20,000.

The macroscopic flow patterns in the wire-wrapped fuel bundle were verified from a comparison with previous studies. The flow

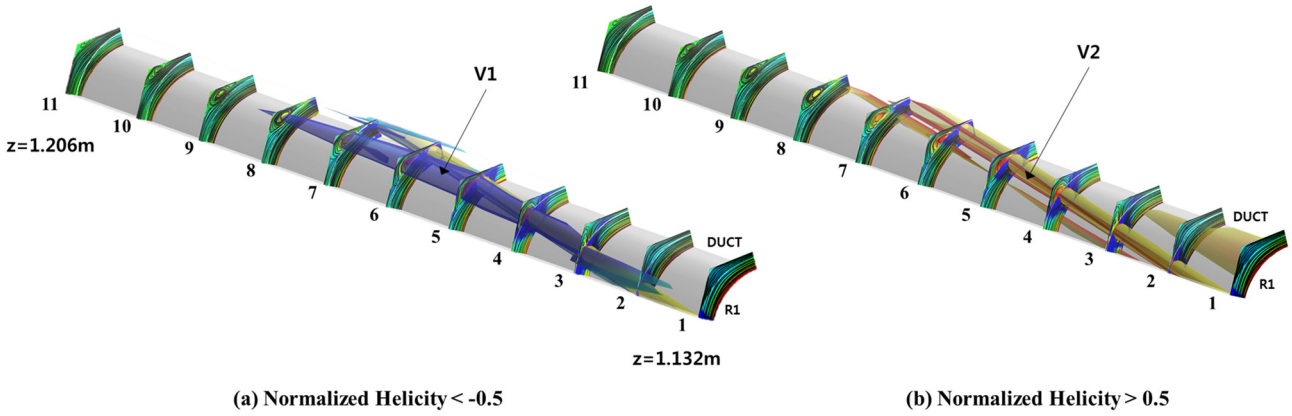

(a) Normalized Helicity < -0.5 (b) Normalized Helicity > 0.5

Fig. 16. Iso-surface of Q-Invariant of 30,000 at the corner subchannel.

region was divided into a peripheral region, where the large swirl flow exists, and an inner region, where the complicated transverse flow exists. Particularly, it was found that the same flow pattern and vortex structures are exhibited when the subchannel type is identical.

Q-invariant and helicity were used to quantify and reconstruct the vortices. In the interior subchannel, three identical vortices were created whenever the wire passes. The direction of transverse flow at the gap depended on the wire position. In the edge subchannel, the wire passed the edge subchannels with two different directions. It was divided into the direction of moving to the interior and to the edge subchannel. When moving to the interior subchannel, a large vortex structure (V1) of the edge subchannel scale was created, and this vortex temporarily blocked the swirl flow. In the corner subchannel, a small-scale vortex trapped in the corners was created, which did not significantly affect the swirl flow in the outer area. In every subchannel, a small vortex (V2) appeared at the lee side of the wire. From the above results, it was found that the scale and flow characteristics of vortices in each subchannel are determined by the relative position of the wire. Applying these findings can improve subchannel codes. The mixing effects of vortices inside subchannels are not properly modeled. Because vortices exist inside each subchannel, subchannel codes can add mixing terms for the momentum and energy in its constitutive equations. For this, further study is necessary to evaluate the mixing effect of vortices.

Acknowledgements

This research was supported by National R&D Program through the National Research Foundation of Korea (NRF) funded by the Ministry of Science, ICT and Future Planning (No. 2016M2B2A9911846) and National Nuclear R&D Program through the National Research Foundation of Korea (NRF) funded by MSIP; Ministry of Science ICT & Future Planning (No. NRF-2013M2B2B1075735).

Nomenclatures

D_P	Pin Diameter [m]
D_W	Wire Diameter [m]
P	Pin Pitch [m]
L_W	Wire Pitch Length [m]
H_T	Total Height of Test Section [m]
ρ	Density [kg/m^3]
μ	Dynamic Viscosity [kg/ms]
Re	Reynolds Number [–]
x, y, z	Cartesian Coordinates [m]
u, v, w	Cartesian Velocity Component [m/s]
u	Velocity Vector [m/s]
f	Friction Factor [–]
ΔP	Pressure Drop [Pa]
D_h	Hydraulic Diameter [m]
$D_{h,\,i}$	Hydraulic Diameter of Interior Subchannel [m]
U	Bulk Velocity [m/s]
U_i	Bulk Velocity in Interior Subchannel [m/s]
L	Distance between Pressure Probes [m]
SST	Shear Stress Transport Model
k – ε	k – epsilon Model
k – ω	k – omega Model
EARSM	Explicit Algebraic Reynolds Stress Model
RNG k – ε	Re-normalization Group k – ε Model
LRRSM	Launder-Reece-Rodi Reynolds Stress Model
V	Volume [–]
H	Helicity [m/s^2]
H_{nor}	Normalized Helicity [–]
Q	Invariant Q [$1/s^2$]
i, j	Component number
Ω_{ij}	Rate of rotation
S_{ij}	Rate of strain

References

[1] N.E. Todreas, L.W. Wilson, Coolant Mixing in Sodium Cooled Fast Reactor Fuel Bundles (No. WASH-1096), Division of Reactor Development and Technology (AEC), Washington, DC, 1968.
[2] R. Ranjan, C. Pantano, P. Fischer, Direct simulation of turbulent heat transfer in swept flow over a wire in a channel, Int. J. Heat Mass Tran. 54 (21–22) (2011) 4636–4654.
[3] J.H. Jeong, M.S. Song, K.L. Lee, Thermal-hydraulic effect of wire spacer in a wire-wrapped fuel bundles for SFR, Nucl. Eng. Des. 320 (2017) 28–43.
[4] J.H. Jeong, M.S. Song, K.L. Lee, RANS based CFD methodology for a real scale 217-pin wire-wrapped fuel assembly of KAERI PGSFR, Nucl. Eng. Des. 313 (2017) 470–485.
[5] R. Gajapathy, K. Velusamy, P. Selvaraj, P. Chellapandi, S.C. Chetal, A comparative CFD investigation of helical wire-wrapped 7, 19 and 37 fuel pin bundles and its extendibility to 217 pin bundle, Nucl. Eng. Des. 239 (11) (2009) 2279–2292.
[6] T. Ohtake, S. Uruwashi, K. Takahashi, Velocity measurements in the subchannel of the wire-spaced subassembly, Nucl. Technol. 30 (3) (1976) 333–349.
[7] M. Nishimura, H. Sato, H. Kamide, H. Ohshima, K. Nagasawa, Y. Imai, Investigation on velocity distribution around the wrapping wire in an inner subchannel of fuel pin bundle, in: 2012 20th International Conference on Nuclear Engineering and the ASME 2012 Power Conference, American Society of Mechanical Engineers, 2012, July, pp. 299–308.
[8] H. Ohshima, Y. Imai, Numerical simulation of flow field in wire-wrapped fuel pin bundle of sodium cooled fast reactor using SPIRAL, Proc. of NTHAS5-F011

(2006) 480–487.
[9] S.K. Chang, D.J. Euh, H.S. Choi, H. Kim, S.R. Choi, H.Y. Lee, Flow distribution and pressure loss in subchannels of a wire-wrapped 37-pin rod bundle for a sodium-cooled fast reactor, Nuclear Engineering and Technology 48 (2) (2016) 376–385.
[10] L. Brockmeyer, L.B. Carasik, E. Merzari, Y. Hassan, Numerical simulations for determination of minimum representative bundle size in wire wrapped tube bundles, Nucl. Eng. Des. 322 (2017) 577–590.
[11] Y.B. Chen, K. Ip, N.E. Todreas, Velocity Measurements in Edge Subchannels of Wire Wrapped LMFBR Fuel Assemblies (No. COO-2245-11TR). Massachusetts Inst. Of Tech, Dept. of Nuclear Engineering, Cambridge (USA), 1974.
[12] J.H. Jeong, J. Yoo, K.L. Lee, K.S. Ha, Three-dimensional flow phenomena in a wire-wrapped 37-pin fuel bundle for SFR, Nuclear Engineering and Technology 47 (5) (2015) 523–533.
[13] J.H. Jeong, M.S. Song, K.L. Lee, CFD investigation of three-dimensional flow phenomena in a JAEA 127-pin wire-wrapped fuel assembly, Nucl. Eng. Des. 323 (2017) 166–184.
[14] ANSYS CFX-Solver Modeling Guide, ANSYS CFX Release 16 (1) (2015).
[15] M.N. Raj, K. Velusamy, Characterization of velocity and temperature fields in a 217 pin wire wrapped fuel bundle of sodium cooled fast reactor, Ann. Nucl. Energy 87 (2016) 331–349.
[16] J. Jeong, F. Hussain, On the identification of a vortex, J. Fluid Mech. 285 (1995) 69–94.